Deformation Monitoring of Slopes With a Shipborne InSAR System: A Case Study of the Lancang River Gorge

TIANWEN LUO[1,2], FEI LI[1], BIN PAN [ID][3], WEI ZHOU[4], HONGJIE CHEN[5], GUANGBAO SHEN[3], AND WEIFENG HAO [ID][6]

[1]State Key Laboratory of Information Engineering in Surveying, Mapping and Remote Sensing, Wuhan University, Wuhan 430079, China
[2]Guizhou Survey and Design Research Institute for Water Resources and Hydropower, Guiyang 550002, China
[3]School of Remote Sensing and Information Engineering, Wuhan University, Wuhan 430079, China
[4]School of Water Resources and Hydropower Engineering, Wuhan University, Wuhan 430072, China
[5]Technology Research and Development Center, Huaneng Lancang River Hydropower Inc., Kunming 650000, China
[6]Chinese Antarctic Center of Surveying and Mapping, Wuhan University, Wuhan 430079, China

Corresponding author: Fei Li (fli@whu.edu.cn)

ABSTRACT Differential synthetic aperture radar interferometry (DInSAR) is a remote sensing technique to monitor ground deformation using repeat-pass data and suitable processing methods. Different platforms have been used to acquire DInSAR data such as space-borne, air-borne, car-mounted, and ground-based SAR systems. Space-borne SAR systems are relatively mature, but air-borne and other systems have attracted increasing interest of the remote sensing community due to their operational flexibility and observation capabilities. In this paper, a new InSAR platform is proposed for the deformation monitoring of reservoir slopes. The shipborne InSAR system uses frequency modulated continuous wave (FMCW) technology with one-transmit-dual-receive configuration. First, we describe the data acquisition process at the Lancang River Bank in October 2019. Subsequently, we present the imaging and interferometric capabilities of the new shipborne InSAR system. Moreover, we analyze the acquired radar data and present an assessment of the quality of the single look complex (SLC) SAR imagery and interferometric products. We focus on the influence of platform stability and baseline bias. Finally, we compare the calculated deformation with the measured deformation obtained from corner reflectors deployed in the monitored area. A line-of-sight error within 2cm is obtained. This paper proposes a novel solution for deformation monitoring of reservoir slopes and a new approach for InSAR applications.

INDEX TERMS Deformation monitoring, frequency-modulated continuous-wave (FMCW), reservoir slopes, SAR interferometry (InSAR), shipborne SAR.

I. INTRODUCTION

Due to the complex geological structure of river slopes, geologic disasters frequently occur, posing a significant threat to the safe operation of hydropower projects [1]. Recently, fast and effective deformation monitoring of reservoir slopes has become a key concern [2].

Differential synthetic aperture radar interferometry (DInSAR) using radar sensors mounted onboard different platforms has become an established technique for detecting and monitoring deformation of the earth's surface, as well as

The associate editor coordinating the review of this manuscript and approving it for publication was Mehmet Alper USLU.

glacier flows and landslides [3]. Space-borne interferometry with a large spatial coverage has been used extensively for monitoring ground-motion with good success [4]–[9]. Although this method is very efficient, the use of space-borne SAR data has several drawbacks, namely, phase artifacts caused by atmospheric effects and very low coherence due to long data acquisition intervals and the short radar wavelength of the sensor [10]. The most significant challenge of DInSAR is errors introduced by variable path delays in the atmosphere [11]. Currently, the best method for mitigating this error source is to acquire a large number of images and perform averaging; however, this may not be possible due to time or cost limitations [12]. Moreover, current space-borne

IEEE *Access*

T. Luo *et al.*: Deformation Monitoring of Slopes With a Shipborne InSAR System: A Case Study of the Lancang River Gorge

sensors are not able to ensure flexible monitoring of critical regions because they are forced to follow polar orbits; thus, they operate only in the South–North (or North–South) direction.

Therefore, different interferometry systems mounted on different platforms have been developed, such as airborne systems [3], [10], [13]–[15], car-borne systems [16]–[19], and ground-based systems [20]–[25]. Airborne and other SAR systems have attracted increasing interest of the remote sensing community due to their operational flexibility and observation capabilities. Among these systems, airborne systems that use frequency-modulated continuous-wave (FMCW) technology are compact and lightweight with a low volume, and have a comparatively low cost. They can be easily mounted on small and highly flexible aerial platforms, such as gliders, helicopters, compound wing aircraft, and unmanned aerial vehicles (UAVs), making them highly attractive. These aerial systems were developed to achieve fast and flexible monitoring and acquire high-resolution data in small areas. The reduction in the size, weight, and costs of the systems are the primary technological challenges in their development. In addition, the main problem of processing airborne SAR data is compensation for the aircraft movement. Uncompensated sensor motion of only half the wavelength (11.3 cm in the L-band) causes a phase error of π [10]. Compared to space-borne or airborne SAR systems, car-borne SAR systems represent a complementary tool in terms of the geometry and the flexibility regarding the choice of location and the temporal baseline [19]. Furthermore, the size of the synthetic aperture is not constrained by the length of a rail, which allows for the use of lower-frequency electromagnetic signals, and are better suited to monitor natural surfaces [19]. Apart from space-borne, airborne, and car-borne radar systems, ground-based radar systems have also been used [20]–[25]. A terrestrial radar interferometer can be used to perform in-situ monitoring of landslides, small glaciers, volcanoes, rock falls, and infrastructure [24]. Moreover, this configuration has several advantages, such as timely measurements that can be obtained from a suitable viewpoint and the repeatability of measurements in both time and space. Terrestrial radar interferometer systems are not limited by the mission design or orbital configuration, and the measurements can be obtained in custom intervals.

Space-borne SAR systems are well suited to illuminate large areas. However, the technological challenge is the implementation of advanced acquisition modes, such as ScanSAR [26]–[29], TOPS [26], [29]–[30], and/or advanced optimization strategies. An example is digital beamforming on receive [31], which is designed to expand the cross-track coverage of the conventional stripmap mode [26]. In contrast, aerial systems, car-borne systems, and ground-based systems are suitable for fast and flexible monitoring to acquire high-resolution data in small areas.

In this paper, a first assessment of the imaging and interferometric capabilities of a shipborne DInSAR system is presented. We describe the acquisition campaign on the Lancang River in Southwest China in 2019. Twelve corner reflectors were deployed in the area illuminated by the radar during the campaign, and very accurate measurements of the induced vertical displacements of the corner reflectors were obtained to acquire a set of reference ground points. The measured deformation of the reference points was compared with the calculated deformation obtained from the shipborne DInSAR system to assess the quality of the SAR imagery and the interferometric products. This study provides references for future research and operational activities with shipborne DInSAR systems.

II. SYSTEM AND DATA
A. SHIPBORNE INSAR SYSTEM
The shipborne InSAR system consists of a dual-polarized active antenna array, power supply unit, display and control unit, high-precision inertial guidance system, stabilization platform, and other components. The system is equipped with three L-band antennas, one of which is transmitting, and the other two are receiving. The one-transmit-dual-receive configuration allows for the simultaneous acquisition of two SAR data sets in a single pass. Three antennas aligned in the cross-track direction allow for the generation of single-pass interferometric products that are not affected by the residual differential errors typical of repeat-pass systems. A stabilization platform with six adjustable axes is used to keep the system at the same level. The axis is raised automatically when it is connected with the power supply. Meanwhile, a three-axis stabilizer is included to prevent the SAR system from rotating horizontally due to wind resistance during operation. Owing to the stabilization platform and three-axis stabilizer, the shipborne InSAR system does not shake violently when the ship sways with the waves, which is crucial for data acquisition using a shipboard SAR system. The system is mounted on the right side of the ship, as shown in Fig. 1c. The rear and side views of the system are shown in Fig. 1a and Fig. 1b, respectively.

The shipborne InSAR system is equipped with a high-precision Differential Global Positioning System/Inertial Measurement Unit (DGPS/IMU) which is connected rigidly to the radar module and is located on the top of stabilization platform, resulting in high stability of the ship's position while recording a track. The main parameters of the DGPS/IMU and the L-band shipborne SAR system are listed in Table 1 and Table 2, respectively. In Table 1, 'Real-time measurement accuracy' means the accuracy of data recorded by the navigation system, and 'Post-processing accuracy' indicates the accuracy after processing by using relative software.

B. DATA ACQUISITION
A section of slope in the Lancang River basin, which is located in Southwest China, was chosen as the monitoring area to evaluate the imaging and interferometric capabilities of the shipborne system, as shown in Fig. 2. The gradient
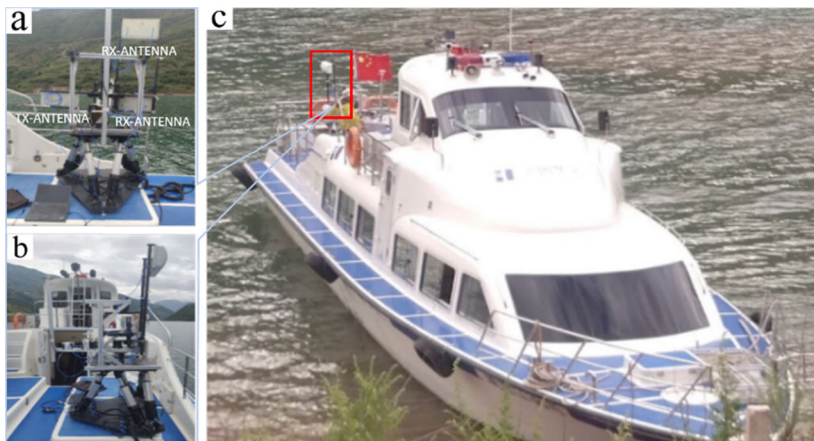
T. Luo *et al.*: Deformation Monitoring of Slopes With a Shipborne InSAR System: A Case Study of the Lancang River Gorge

IEEE *Access*

FIGURE 1. The shipborne InSAR system and the platform. The system consists of the SAR host, POS system, radar antenna, control equipment, stable platform, and power supply. (a) Rear view of the system. (b) side view of the system. (c) The system is mounted on a 1 m × 2 m platform on the right side of the stern.

TABLE 1. Main parameters of the DGPS/IMU navigation system.

	Real-time measurement accuracy (1 σ)	Post-processing accuracy (1 σ)
Heading measurement accuracy (°)	0.02	0.005
Attitude measurement accuracy (°)	0.005	0.002
Position measurement accuracy (m)	3~5	0.02 (Horizontal) 0.05 (Height)
Speed measurement accuracy (m/s)	0.05	0.03

TABLE 2. Main Parameters of the L-band SAR system.

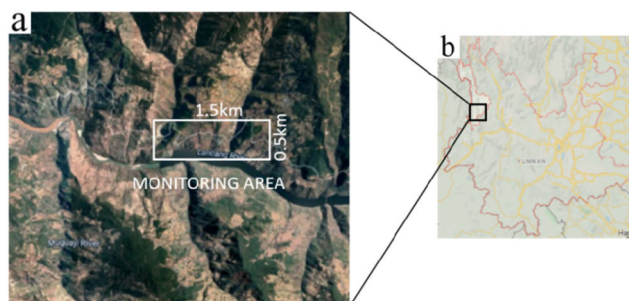|	
Frequency	1.325 GHz
Wavelength	22.6 cm
Signal broadband	100 MHz
Ship speed	~7.5 m/s
Antenna length (azimuth, range)	0.4 m, 0.1 m
Pulse repetition frequency	1400 Hz
Beam center angle	40°
Polarization	Full polarization
Radar transmit power	1000 W
Maximum recordable range	6 km
Number of antennas	3

FIGURE 2. The monitoring area (1.5 km long and 0.5 km wide) in Lanping County, Nujiang Autonomous Prefecture, Yunnan Province, China. The dominant classes in the area are bare soil, grassland, and small rocks. (a) Location of the monitoring area on the Google Maps. (b) The location of the monitoring area on a small scale map.

of the area changes slowly, which reduces the overlap and shadow areas in the SAR imagery. The slant range is about 500m, and the heading of the ship is perpendicular to the beam. Small rocks and the trihedral corner reflectors in the monitored area exhibit strong scattering in the SAR imagery and can be used as reference points for deformation calculation.

Figure 3 shows the design diagram of the ship's trajectory. The InSAR system operates in Section AB. A single track is 1.5 km long, which is also the azimuth length of the SAR

imagery. The beam center angle of the antenna is 40°, and the lowest and highest radar waves hit the water and slope, respectively. Corner reflectors are used to assess the accuracy of the proposed method. The corner reflectors layout and the SAR imaging area are shown in Fig. 3. Twelve three-sided corner reflectors with a side length of 0.4 m are deployed in the monitored area; all reflectors face the route direction, as shown in Fig. 3b. Moreover, vertical displacement corresponding to different ratios of the wavelength in the slant range direction is manually induced on each corner reflector before the start of the image acquisition. The measurement
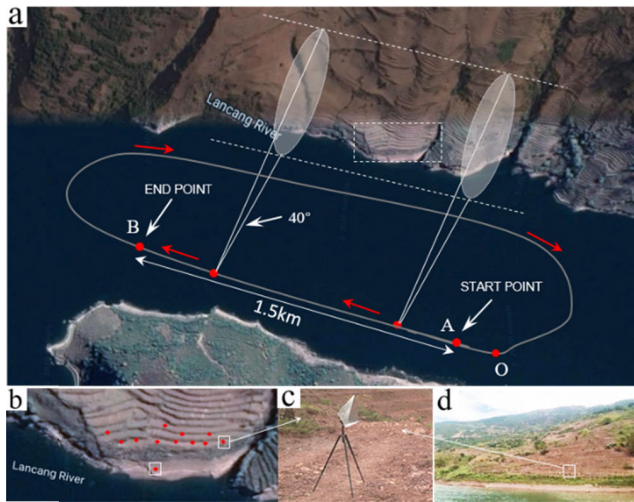
FIGURE 3. Design diagram of the shipborne SAR data acquisition campaign. (a) Point O is the point where the ship starts to move, and section AB is where the SAR system is operating. The length of the single track is about 1.5 km, and the speed of the ship is about 7.5 m/s. (b) The area where the corner reflectors are deployed. (c) A corner reflector deployed in the monitored area. (d) Photo of the monitored area taken on the day of the campaign.

of the vertical displacement of the corner reflectors allows us to evaluate the accuracy of the deformation obtained from the differential interferograms. One corner reflector is placed near the river, and shows whether the SAR imagery is focused well. Fig. 3c shows a photo of a corner reflector deployed in the monitored area, and Fig. 3d shows a photo of the monitored area taken on the day of the campaign.

The interferometry baseline of the repeat track should be as small as possible to obtain highly accurate differential interferometry results. An experienced captain was able to ensure that the baselines between different tracks will not change sharply. Figure 4 shows the tracks recorded by GPS; Fig. 4a shows the records for the entire path and Fig. 4b shows a magnification of parts of Fig. 4a (the red rectangle in Fig. 4a), denoting the ship's trajectory during the working hours of the SAR system. The distance between the different trajectories is controlled within 1~2 m, and the ship's track is in a straight line.
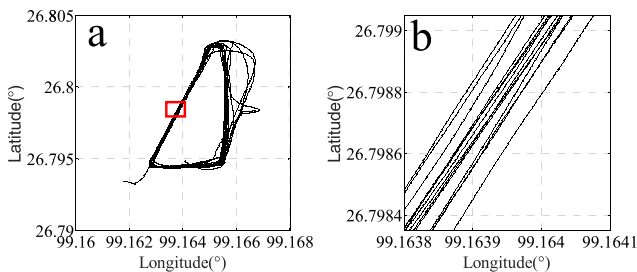

FIGURE 4. The tracks of the ship recorded by GPS for (a) the entire trajectory of the ship and (b) for the portion shown in the red rectangle in (a). The ship's trajectory is shown during the working hours of the InSAR system.

Figure 5 shows the SAR imagery obtained from a single pass. Fig. 5a and Fig. 5b show the data acquired by the
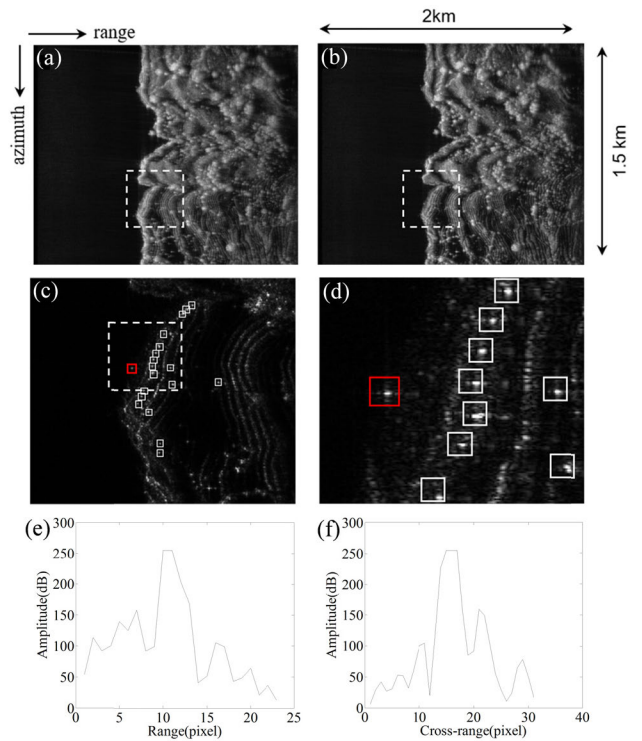

FIGURE 5. (a)(b) Single look SAR imagery obtained from a single pass. Both images are 2 km in range and 1.5 km in the azimuth. The black area on the left of the imagery is water, and the grey area on the right is the monitored area. (c) Enlarged view of the white square area in Fig. 5a. The point in the red square represents the corner reflector deployed near the Lancang River. The smaller white squares are the reference points, which show strong scattering. (d) The enlarged area of the largest white square in Fig. 5c shows that the imagery acquired by the shipborne system is well focused. (e)(f) A range and cross-range cut of the isolated corner reflector (in the red square) shows the focusing quality of shipborne SAR images.

receiving antennas in Fig. 1. Both images are 2 km in range and 1.5 km in the azimuth. The texture of the monitored area is visible in the imagery, and the gradient can be observed. Fig. 5c is the enlarged view of the square area in Fig. 5a. The red square in Fig. 5c is the corner reflector deployed near the Lancang River. The smaller white squares are the reference points, which exhibit strong scattering. The red square in Fig. 5d is the same corner reflector that is shown in Fig. 5c, demonstrating that the imagery acquired by the shipborne system is well focused. Figure 5 shows only one of the seven SAR imagery pairs that were acquired in this case. All images were well- focused. A range and cross-range cut of a corner reflector is shown in the Figure 5e and 5f. To evaluate the focusing quality, we picked one of the CRs and showed the range and cross-range cut of the scatter. These figures are the SAR image and corresponding range cut and cross-range cut of the isolated point-like scatter. The Figure 5e and 5f show that the shipborne-InSAR system is capable of acquiring well-focused SAR images.

III. METHODOLOGY
The baselines of the multi-pass data should be as small as possible to obtain high-precision deformation results.

T. Luo *et al.*: Deformation Monitoring of Slopes With a Shipborne InSAR System: A Case Study of the Lancang River Gorge
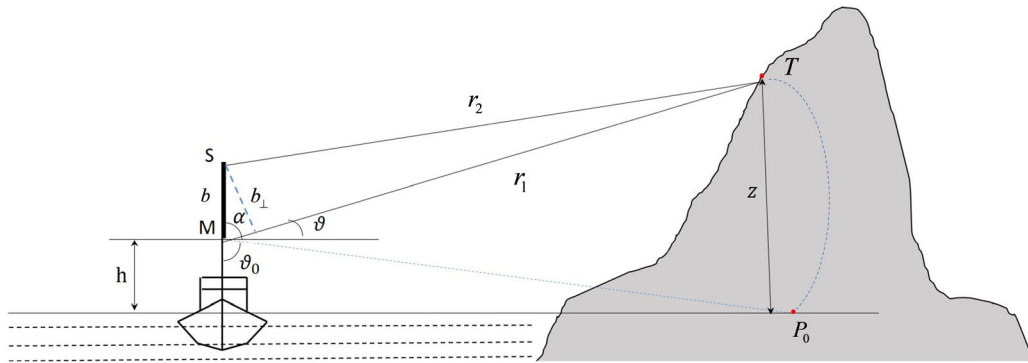
IEEE *Access*

FIGURE 6. Geometric model of the interferometry of the shipborne InSAR system.

Therefore, we used the data of two passes with a short baseline as an interferometric pair and the single pass as another interferometric pair.

The complex signal can be written as:

$$u = |u|\, e^{j\varphi} = u e^{j2\pi(ct-2r)\varphi/\lambda} e^{j\varphi_{scat}} \quad (1)$$

where the φ is the phase value of the complex signal, t is the time variable, u is the amplitude, r is the distance from the ground target to the SAR sensor, c is the velocity of electromagnetic waves, λ is the wavelength and φ_{scat} represents the contribution from the scattering phase of the target. Assuming that the electromagnetic-wave scattering mechanism on the ground has not changed between the two acquisitions and a SAR interferogram can be obtained by complex conjugate multiplication of two co-registered SAR images u_1, u_2. The obtained intimal Interferometric phase φ is the composite of topographic phase φ_{topo}, flat-earth phase φ_{ref}, displacement phase φ_{disp} and noise φ_{noise}, which includes atmospheric noise and electronic noise.

$$\varphi = (u_1 u_2^*) = \varphi_1 - \varphi_2 = -\frac{4\pi}{\lambda}\delta_r$$
$$= \varphi_{topo} + \varphi_{atm} + \varphi_{ref} + \varphi_{disp} + \varphi_{noise} \quad (2)$$
$$\delta_r = r_1 - r_2 \quad (3)$$

where * denotes complex conjugate, φ_1 and φ_2 is the phase value of the complex signal on SAR images, δ_r is the range change of the ground target to the SAR sensor of the two acquisitions.

The geometric model of the shipborne SAR system is shown in Fig.6. S and M represent two receiving antennas' positions, b is defined as baseline, α represents the angle between baseline and horizontal surface, ϑ is the look angle, r_1 and r_2 are the slant distance between the antenna and ground target. Taking into account the imaging geometry illustrated in Fig.6 and the application of the cosine's rule to the MST triangle depicted in Fig.6, it is straightforward to demonstrate that:

$$r_2 = \sqrt{b^2 + r_1^2 - 2br_1 \sin(\alpha - \vartheta)} \simeq r_1 - b\sin(\alpha - \vartheta) \quad (4)$$

The interferometric phase can be written as:

$$\varphi = -\frac{4\pi}{\lambda}\delta_r \simeq -\frac{4\pi}{\lambda}b\sin(\alpha - \vartheta) = -\frac{4\pi}{\lambda}b_{//} \quad (5)$$

where $b_{//}$ is the parallel baseline component.

Let us refer to the geometry of the problem sketched in Fig.6 and we expand Equation (4) around the angular position $\vartheta = \vartheta_0$, which represents the side looking angle that corresponds to the case when Earth's surface is flat (i.e. $z=0$). Since the monitored area in this study is quite small, we believe that the assumption of the flat Earth's surface is reasonable.

$$\sin(\alpha - \vartheta) = \sin[(\alpha - \vartheta_0) + (\vartheta_0 - \vartheta)] = \sin(\alpha - \vartheta_0)$$
$$+ (\vartheta_0 - \vartheta)\cos(\alpha - \vartheta_0) \quad (6)$$

The target height, namely z, is related to the side-looking angle ϑ and to the antenna height h as

$$z = h + r_1 \cos\vartheta \quad (7)$$

Hence:

$$\frac{\partial z}{\partial \vartheta} = -r_1 \sin\vartheta \rightarrow \frac{\partial \vartheta}{\partial z}$$
$$= -\frac{1}{r_1 \sin\vartheta} \rightarrow (\vartheta_0 - \vartheta) = -\frac{z}{r_1 \sin\vartheta} \quad (8)$$

Finally, the interferometric phase can be seen as composed three distinctive terms, as follows:

$$\varphi \simeq \underbrace{-\frac{4\pi}{\lambda}b\sin(\alpha - \vartheta_0)}_{\varphi_{ref}} + \underbrace{\frac{4\pi}{\lambda}\frac{b_\perp}{r_1 \sin\vartheta}z}_{\varphi_{topo}} + \underbrace{\frac{4\pi}{\lambda}D}_{\varphi_{disp}} \quad (9)$$

where D is the displacement along the line of sight (LOS), and the mathematical relation $b_\perp = b\cos(\alpha - \vartheta_0)$ has been used.

DInSAR requires the removal of the phase signatures of the flat-earth and topography to isolate the ground displacement component. After removing the flat earth phase φ_{ref} [31], the flattened interferogram φ_f can be obtained and expressed as:

$$\varphi_f = \frac{4\pi}{\lambda}\frac{b_\perp}{r_1 \sin\vartheta}z + \frac{4\pi}{\lambda}D \quad (10)$$

IEEE *Access*

T. Luo *et al.*: Deformation Monitoring of Slopes With a Shipborne InSAR System: A Case Study of the Lancang River Gorge

Equation (10) is the basic equation for measuring ground movement using the DInSAR technique. In this study, repeat-pass SAR images were used to obtain two flattened interferograms with respect to the reference SAR image. One interferogram is called the deformation pair (defo-pair) and the other is called the topographic pair (topo-pair):

$$
\begin{cases}
\varphi_f^{dp} = \dfrac{4\pi}{\lambda}\dfrac{b_\perp^{dp}}{r^{dp}\sin\vartheta^{dp}}z + \dfrac{4\pi}{\lambda}D^{dp} \\[2ex]
\varphi_f^{tp} = \dfrac{4\pi}{\lambda}\dfrac{b_\perp^{tp}}{r^{tp}\sin\vartheta^{tp}}z + \dfrac{4\pi}{\lambda}D^{tp}
\end{cases} \tag{11}
$$

where d_p means deformation pair and t_p means topographic pair. From Equation (11), the term representing displacement can be written as:

$$
D^{dp} = \frac{\lambda}{4\pi}\varphi_f^{dp} - \frac{\lambda}{4\pi}\frac{b_\perp^{dp}r^{tp}\sin\vartheta^{tp}}{b_\perp^{tp}r^{dp}\sin\vartheta^{dp}}\left(\varphi_f^{tp} - \frac{4\pi}{\lambda}D^{tp}\right) \tag{12}
$$

In this study, we assume that there is no displacement during the acquisition time of the topo-pair SAR images; that is to say that the displacement term D^{tp} in Equation (12) is zero. Since in this paper, we use two-antenna shipborne InSAR system, and the monitored area does not have any deformation during the acquiring time, so we assume that the D^{tp} in this study is 0, and then we could get the deformation information in the defo-pair images.

IV. RESULTS AND ANALYSIS

A. RESULTS

Differential interferometry requires two interferometric pairs, i.e., one pair at the same time and one pair at different times. Six interferometric pairs are used in this study, and we use the results of one pair as an example. The baselines of all six pairs are within 2 m, and some are within 1 m. The single-pass and multi-pass results are shown in Fig. 7 and Fig. 8. Figure 7a and b show the interferogram and coherence map of the single-pass SAR imagery. The interferogram shows the results of the single-pass SAR imagery pairs. The coherence map reflects the data quality, and Fig. 7b shows that the single-pass data have good coherence. However, several linear regions in Fig. 7b have low coherence. Combined with the analysis of Fig. 3, we believe that shrub areas and the edges of the gradients are the low-coherence areas.
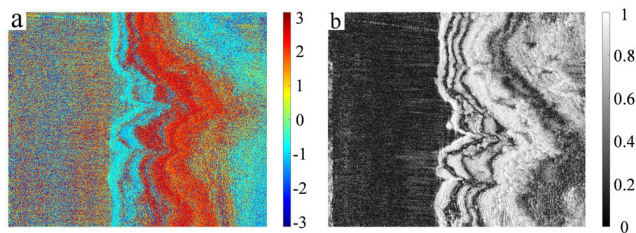

FIGURE 7. Processing results of the single-pass SAR imagery, (a) and (b) are the interferogram and coherence map, respectively. The phase of the water area in (a) is meaningless, and the corresponding area in (b) has low coherence. Most of the monitored area has good coherence, which facilitates differential interferometry processing.
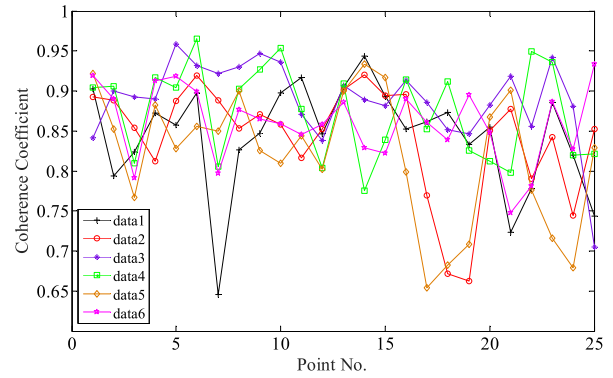

FIGURE 8. There are total 25 points chosen to analysis the accuracy of the result, and 14 of them (No. 2, No.3, No.5, No.6, No.7, No.8, No.10, No.11, No.14, No.16, No.17, No.19, No.24, No.25) are natural permanent scatterers and 11 of them (No.1, No.4, No.9, No.12, No.13, No.15, No.18, No.20, No.21, No.22, No.23) are CRs. Coherence coefficients of the permanent scatterers were used to calculate the deformation data. All six interferometric pairs are chosen based on the principle that a smaller baseline is preferred. Almost all points have high coherence, and the coherence coefficients fluctuate around 0.85. Eight coherence coefficients are relatively low (between 0.6 and 0.7).

The single-pass data shows that the L-band shipborne InSAR system can acquire imagery with high coherence. High-quality single-pass and multi-pass data are required to obtain deformation information. Instead of showing the coherence map, we present the coherence coefficients of the 25 reference points (12 are corner reflectors placed in the monitored area, and 13 are objects with stable scattering characteristics, such as rocks and stone piers). As shown in Fig. 8, all 25 points of the 6 interferometric pairs have coherence coefficients higher than 0.65. Most of the coherence coefficients fluctuate around 0.85. In this study, the deformation is calculated based on these points. The above analysis shows that these points have high-quality coherence, which improves the reliability of the deformation results.

Based on the phase of the single-pass and multi-pass data, we obtain the deformation values of 25 points using the model described in Section 3. However, the phase of the interferogram is not the real phase that represents the slant distance between the target and the antenna but is the wrapped phase. The wrapped phase has to be unwrapped to calculate the deformation. In this study, we use the 'branch cut' algorithm [32] to unwrap the phase of all the permanent scatterers. First, we determine whether a point is a residual point. If it is a residual point, we remove this point and find a new one in its neighborhood. We repeat the first step until no more residual points exist. Then we unwrap the phase based on the principle that the phase of two adjacent pixels should not exceed π. If it exceeds π, we subtract π, and if it exceeds $-\pi$, we add π. After unwrapping, we obtain the relative phase value, which means that the phase is continuous in the image space but does not represent the real distance between the target and the antenna. However, the deformation (line of sight) of all points in this study is within half a wavelength (the deformation of the 12 corner reflectors is adjusted to

T. Luo *et al.*: Deformation Monitoring of Slopes With a Shipborne InSAR System: A Case Study of the Lancang River Gorge

IEEE *Access*

within 5 cm, and the deformation of the 13 permanent scatters is 0), which means that phase used to obtain the deformation is within π. Therefore, the phase after unwrapping can be used to calculate the deformation. The baseline of each interferometric pair is estimated with orbital trajectories with decimeter accuracy. Finally, the deformation of the 25 points is determined using the proposed model. The details of this procedure are illustrated in Fig. 9.
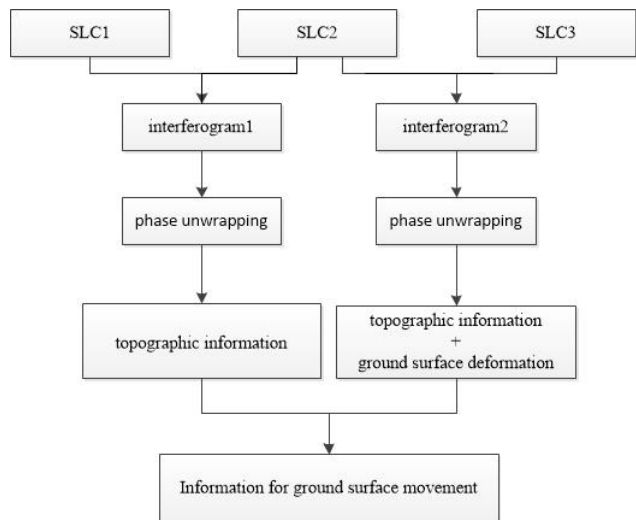

FIGURE 9. Flow diagram of the DInSAR processing chain.

The processing results of the single-pass and multi-pass SAR imagery and the analysis of the data indicate that the phase and baseline used to obtain the deformation are reliable. A set of 6 imagery pairs with the spatial baseline is selected to produce the interferograms and create different interferometric pairs with the single-pass data. We compare the results with the deformation obtained from the ground measurements to determine the accuracy of the proposed method. The differences of the deformation values obtained from the two methods are presented in Fig. 10. Both values represent line-of-sight deformations. We refer to the results as measured deformation and calculated deformation. As shown in the diagram, the deformation obtained from the two methods differs at different points. The difference of deformation is relatively large (4 cm) at some points, such as No. 4 and No. 9 in the first group and No. 9 in the third group. The deformation difference of No. 4 in the 6th group exceeds 4 cm. On the other hand, some points have relatively small differences (less than 0.1 cm), for example, No. 16 and No. 24 in the first group and No. 12 and No. 13 in the third group. The differences at most of the points range from 0.5 cm to 1.5 cm. The root mean square error (RMSE) of the groups is listed in Tab. 3. The 4th group has the lowest RMSE (0.865), and the 3rd group has the highest RMSE (1.846). The baseline of the interferometric pairs and average coherence coefficients are also listed to show their influence on the deformation results. The 3rd group has the lowest baseline (0.067 m), but its RMSE is the highest. The average coherence coefficient of the 2nd group

TABLE 3. Statistics of the deformation results.

	1	2	3	4	5	6
Baseline (m)	1.012	0.603	0.067	1.477	1.364	1.631
Average Coherence Coefficient	0.844	0.889	0.843	0.873	0.820	0.859
RMSE (cm, line of sight)	1.635	1.238	1.846	0.865	1.83	1.723

is the highest, but its RMSE is not. We provide a detailed analysis of the influence of the baseline and coherence on the deformation results in Section B.

B. ANALYSIS

In this section, we describe a detailed analysis of the deformation results to determine the factors contributing to errors during the entire process from data acquisition to deformation calculation. We also discuss potential methods to reduce the error. First, after acquiring the data with the L-band shipborne InSAR system, we used the raw data and base station GPS data combined with the trajectory data recorded by the POS system prior to image analysis. Although the images shown in Fig. 5 indicate that the SAR data are well focused, the data are affected by thermal noise, which introduces errors in the phase. Second, the accuracy of the registration must be within 0.1 pixel [34] to avoid a phase error due to registration. In this study, the coherence coefficient algorithm is used for registration, and bilinear interpolation is performed. The results in section A show that both the single-pass and multi-pass data have high coherence. However, at some points of low coherence, phase errors due to registration are inevitable. Moreover, the estimation of the horizontal component of the spatial baseline in the model (Section III) will result in errors. A small deviation exists in the data recorded by the POS system, which is used to calculate the spatial baseline, and some deviation in the incident angles of the points cannot be avoided. Both deviations cause spatial baseline errors, which further result in deformation errors. Finally, since we did not have an accurate value of the distance, the phase obtained by phase unwrapping is only continuous in the imagery space, and it is not an absolute value but a relative value. Although the absolute phase value is not required to calculate the deformation (a detailed analysis is given in Section A), if the starting point of unwrapping has an error, the error will propagate to the imagery, causing a global error. All points that were used to calculate the deformation has some deviation. In summary, a high-precision POS system is needed to calculate the baseline to reduce the errors. The incident angle should be chosen to avoid overlap and shadow areas in the SAR imagery to prevent the creation of residual points in the unwrapping phase.

V. DISCUSSION

In this study, data acquisition and analysis of a novel shipborne InSAR system are described. Single-pass and multi-pass SAR imagery is used to produce interferometric pairs. The deformation obtained from the proposed model is
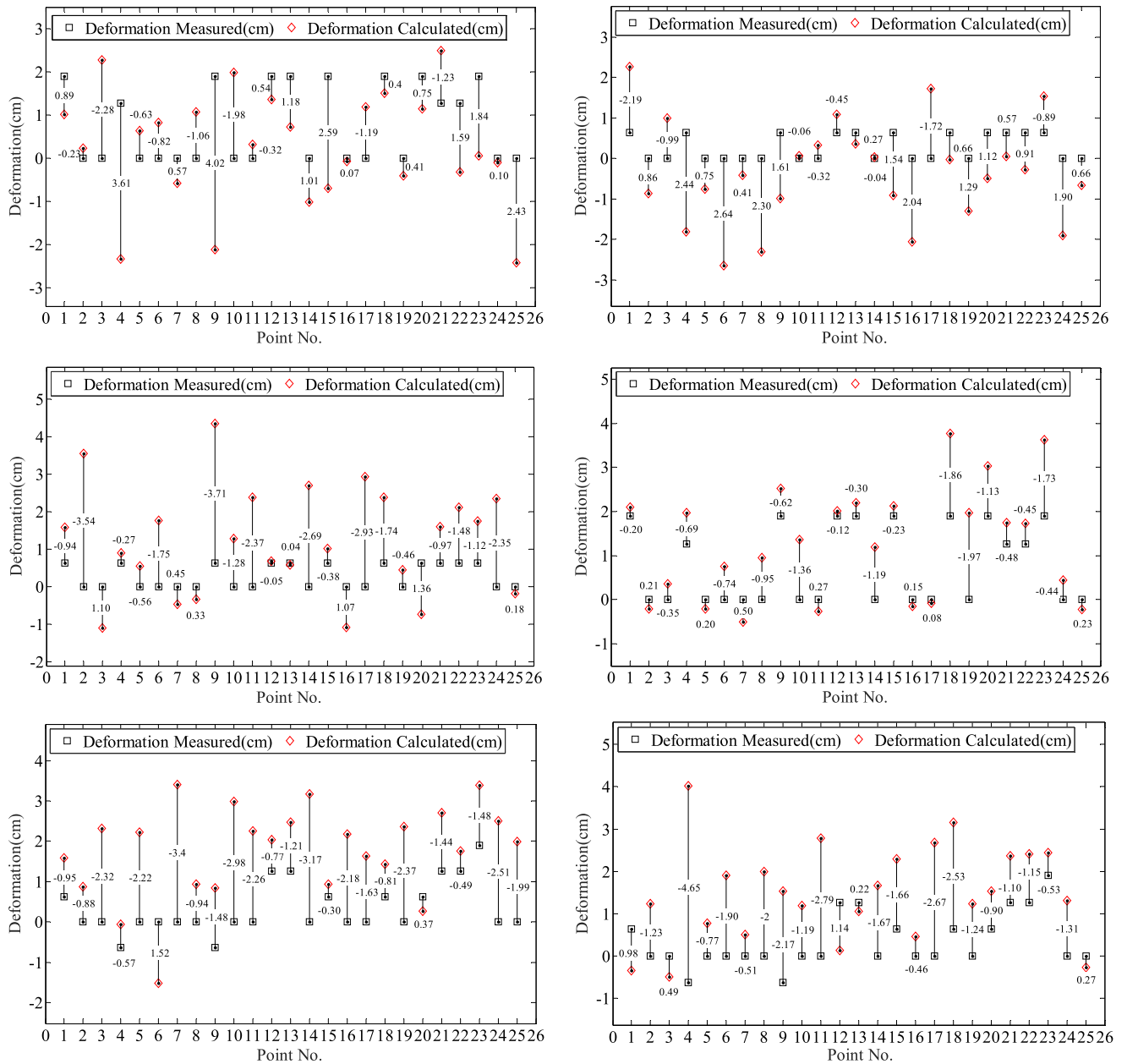
IEEE *Access*

T. Luo *et al.*: Deformation Monitoring of Slopes With a Shipborne InSAR System: A Case Study of the Lancang River Gorge

FIGURE 10. Deformation of 25 points obtained from ground measurements (black squares) and from the proposed method (red diamonds). The differences between the two deformation values are indicated. The longer the vertical line, the greater the difference is. There are total 25 points chosen to analyze the accuracy of the results, and 14 of them are natural permanent scatterers and 11 of them are CRs (same as fig. 8).

compared with the measured deformation. Here, we discuss the problems we encountered in this process. Since the shipborne system operates on an unstable water surface, it is challenging to maintain the stability of the system. We analyze the trajectories recorded by the GPS to evaluate the stability of the shipborne SAR system during the operation.

Figure 11 shows the tracks depicted in Fig. 4a from a different perspective. The red rectangle in Fig. 11a is the operating area of the InSAR system. This area is the most stable area during the entire data collection process. Figure 11b shows the magnification of the red rectangle.

The maximum fluctuation does not exceed 0.1 m, and most values are within 0.05 m. Since the vertical accuracy of the GPS is 0.05 m, we conclude that the shipborne InSAR system has relatively high stability on the water, which is important to acquire well-focused SAR imagery.

Most SAR images mentioned above were well focused; however, we provide an example of a badly-focused image (Fig. 12). Figure 12a shows the HH polarization amplitude imagery; the texture of the objects is not clear. The coherence map (Fig. 12b) shows that most of the pixels do not have high coherence. Even though the trajectory (Fig. 11a) shows
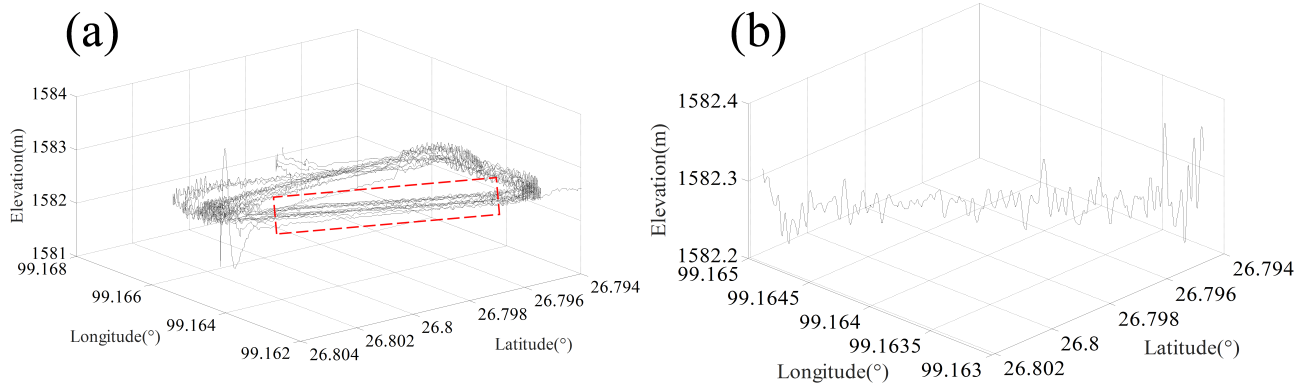
T. Luo *et al.*: Deformation Monitoring of Slopes With a Shipborne InSAR System: A Case Study of the Lancang River Gorge

IEEE *Access*

FIGURE 11. Trajectories recorded by GPS. (a) The entire trajectory of the ship during data acquisition. The red rectangle marks the area where the InSAR system was operated. (b) Magnification of one of the trajectories in the red rectangle area in (a). Both fig. 3 and fig. 11 are plotted with POS data, and fig.11 shows the elevation information to show the stability of the shipborne InSAR system during the working time.
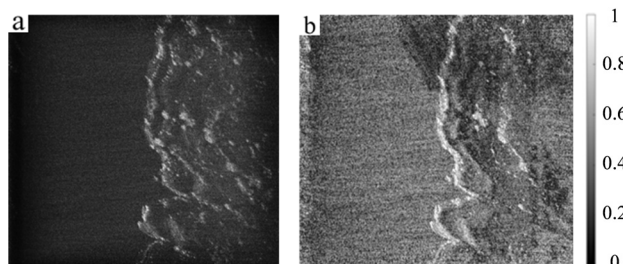

FIGURE 12. Example of a badly-focused HH polarization amplitude image (a) and its coherence map (b). The SAR amplitude imagery shows that the texture of the objects is not clear. Most of the pixels have low coherence.

that the system operates stably, bad-focused imagery does occur. Small differences between the trajectories may lead to images with different qualities. A higher-precision POS is needed to compare the trajectory differences of images with different qualities. The results indicate that the shipborne InSAR system operates stably, although a higher-precision POS is needed to determine the small differences between the trajectories.

VI. CONCLUSION

In this work, we presented the imaging and interferometric capabilities of a shipborne single-pass L-band InSAR system. The long wavelength and high coherence of the L-band allow for the analysis of long-term processes in vegetated areas. In addition, the capabilities for monitoring short-term processes are improved by the greater flexibility of shipborne sensors.

We conducted an image acquisition campaign on the Lancang River in Southwest China in 2019. Interferometric pairs were obtained from single-pass and multi-pass imagery to calculate the deformation using the proposed model. Corner reflectors deployed in the area and other strong scattering targets were used as reference points. We assessed the quality of the SAR imagery and InSAR products by comparing the measured and calculated deformation values. A line-of-sight

mean error within 2 cm was obtained. An analysis of the error source was presented, and methods to reduce the error were provided.

The results provide a reference for future research and operational activities with this system and demonstrate the imaging and interferometric capabilities of the shipborne L-band InSAR system. The shipboard system is well adapted to the water environment and provides a flexible and fast data acquisition method. More generally, the results show that the shipborne infrastructure system (which consists of the radar system and the complete data processing chain from raw data acquisition to the generation of deformation products) may represent an appealing monitoring solution for applications that require operating on the water for obtaining high-resolution InSAR products.

REFERENCES

[1] A. Carrara, F. Guzzetti, M. Cardinali, and P. Reichenbach, "Use of GIS technology in the prediction and monitoring of landslide hazard," *Natural Hazards*, vol. 20, nos. 2–3, pp. 117–135, 1999.

[2] A. Bhattacharya, K. Mukherjee, M. Kuri, M. Vöge, M. L. Sharma, M. K. Arora, and R. K. Bhasin, "Potential of SAR intensity tracking technique to estimate displacement rate in a landslide-prone area in haridwar region, India," *Natural Hazards*, vol. 79, no. 3, pp. 2101–2121, Dec. 2015.

[3] C. Esposito, A. Natale, G. Palmese, P. Berardino, R. Lanari, and S. Perna, "On the capabilities of the italian airborne FMCW AXIS InSAR system," *Remote Sens.*, vol. 12, no. 3, p. 539, Feb. 2020.

[4] M. Lazecky, I. Hlavacova, M. Bakon, J. J. Sousa, D. Perissin, and G. Patricio, "Bridge displacements monitoring using space-borne X-band SAR interferometry," *IEEE J. Sel. Topics Appl. Earth Observ. Remote Sens.*, vol. 10, no. 1, pp. 205–210, Jan. 2017.

[5] C. Colesanti and J. Wasowski, "Investigating landslides with spaceborne synthetic aperture radar (SAR) interferometry," *Eng. Geol.*, vol. 88, nos. 3–4, pp. 173–199, Dec. 2006.

[6] D. Closson, N. A. Karaki, H. Hansen, D. Derauw, C. Barbier, and A. Ozer, "Space-borne radar interferometric mapping of precursory deformations of a dyke collapse, dead sea area, Jordan," *Int. J. Remote Sens.*, vol. 24, no. 4, pp. 843–849, Jan. 2003.

[7] A. K. Gabriel, R. M. Goldstein, and H. A. Zebker, "Mapping small elevation changes over large areas: Differential radar interferometry," *J. Geophys. Res.*, vol. 94, pp. 9183–9191, Jul. 1989.

IEEE Access·

T. Luo *et al.*: Deformation Monitoring of Slopes With a Shipborne InSAR System: A Case Study of the Lancang River Gorge

[8] A. Ferretti, C. Prati, and F. Rocca, "Nonlinear subsidence rate estimation using permanent scatterers in differential SAR interferometry," *IEEE Trans. Geosci. Remote Sens.*, vol. 38, no. 5, pp. 2202–2212, 2000.

[9] D. Massonnet, M. Rossi, C. Carmona, F. Adragna, G. Peltzer, K. Feigl, and T. Rabaute, "The displacement field of the landers earthquake mapped by radar interferometry," *Nature*, vol. 364, no. 6433, pp. 138–142, Jul. 1993.

[10] A. Reigber and R. Scheiber, "Airborne differential SAR interferometry: First results at l-band," *IEEE Trans. Geosci. Remote Sens.*, vol. 41, no. 6, pp. 1516–1520, Jun. 2003.

[11] Z.-W. Li, X.-L. Ding, J.-J. Zhu, and Z.-R. Zou, "Quantitative study of atmospheric effects in spaceborne InSAR measurements," *J. Central South Univ. Technol.*, vol. 12, no. 4, pp. 494–498, Aug. 2005.

[12] A. Ferretti, G. Savio, R. Barzaghi, A. Borghi, S. Musazzi, F. Novali, C. Prati, and F. Rocca, "Submillimeter accuracy of InSAR time series: Experimental validation," *IEEE Trans. Geosci. Remote Sens.*, vol. 45, no. 5, pp. 1142–1153, May 2007.

[13] A. Reigber and A. Moreira, "First demonstration of airborne SAR tomography using multibaseline L-band data," *IEEE Trans. Geosci. Remote Sens.*, vol. 38, no. 5, pp. 2142–2152, 2000.

[14] G. Fornado, "Trajectory deviations in airborne SAR: Analysis and compensation," *IEEE Trans. Aerosp. Electron. Syst.*, vol. 35, no. 3, pp. 997–1009, Jul. 1999.

[15] A. Moreira and Y. Huang, "Airborne SAR processing of highly squinted data using a chirp scaling approach with integrated motion compensation," *IEEE Trans. Geosci. Remote Sens.*, vol. 32, no. 5, pp. 1029–1040, 1994.

[16] O. Frey, C. L. Werner, U. Wegmuller, A. Wiesmann, D. Henke, and C. Magnard, "A car-borne SAR and InSAR experiment," in *Proc. IEEE Int. Geosci. Remote Sens. Symp. (IGARSS)*, Melbourne, VIC, Australia, Jul. 2013, pp. 93–96.

[17] O. Frey, C. L. Werner, I. Hajnsek, and R. Coscione, "A car-borne SAR system for interferometric measurements: Development status and system enhancements," in *Proc. IEEE Int. Geosci. Remote Sens. Symp. (IGARSS)*, Valencia, Spain, Jul. 2018, pp. 6508–6511.

[18] O. Frey, C. L. Werner, and R. Coscione, "Car-borne and UAV-borne mobile mapping of surface displacements with a compact repeat-pass interferometric SAR system at L-band," in *Proc. IEEE Int. Geosci. Remote Sens. Symp. (IGARSS)*, Yokohama, Japan, Jul. 2019, pp. 274–277.

[19] R. Coscione, I. Hajnsek, and O. Frey, "An experimental car-borne SAR system: Measurement setup and positioning error analysis," in *Proc. IEEE Int. Geosci. Remote Sens. Symp. (IGARSS)*, Valencia, Spain, Jul. 2018, pp. 6364–6367.

[20] G. Antonello, N. Casagli, P. Farina, D. Leva, G. Nico, A. J. Sieber, and D. Tarchi, "Ground-based SAR interferometry for monitoring mass movements," *Landslides*, vol. 1, no. 1, pp. 21–28, Mar. 2004.

[21] D. Leva, G. Nico, D. Tarchi, J. Fortuny-Guasch, and A. J. Sieber, "Temporal analysis of a landslide by means of a ground-based SAR interferometer," *IEEE Trans. Geosci. Remote Sens.*, vol. 41, no. 4, pp. 745–752, Apr. 2003.

[22] D. Tarchi, N. Casagli, R. Fanti, D. D. Leva, G. Luzi, A. Pasuto, M. Pieraccini, and S. Silvano, "Landslide monitoring by using ground-based SAR interferometry: An example of application to the tessina landslide in italy," *Eng. Geol.*, vol. 68, nos. 1–2, pp. 15–30, Feb. 2003.

[23] O. Monserrat, M. Crosetto, and G. Luzi, "A review of ground-based SAR interferometry for deformation measurement," *ISPRS J. Photogramm. Remote Sens.*, vol. 93, pp. 40–48, Jul. 2014.

[24] C. Werner, T. Strozzi, A. Wiesmann, and U. Wegmuller, "A real-aperture radar for ground-based differential interferometry," in *Proc. IEEE Int. Geosci. Remote Sens. Symp. (IGARSS)*, Boston, MA, USA, Jul. 2008, pp. III-210–III-213.

[25] C. Werner, A. Wiesmann, T. Strozzi, and U. Wegmuller, "The GPRI multimode differential interferometric radar for ground-based observations," in *Proc. 9th Eur. Conf. Synth. Aperture Radar (EUSAR)*, Nuremberg, Germany, 2012, pp. 304–307.

[26] G. Franceschetti and R. R. Lanari, *Synthetic Aperture Radar Processing*. Boca Raton, FL, USA: CRC Press, 1999, pp. 15–64.

[27] A. Moreira, P. Prats-Iraola, M. Younis, G. Krieger, I. Hajnsek, and K. P. Papathanassiou, "A tutorial on synthetic aperture radar," *IEEE Geosci. Remote Sens. Mag.*, vol. 1, no. 1, pp. 6–43, Mar. 2013.

[28] K. Tomiyasu, "Conceptual performance of a satellite borne, wide swath synthetic aperture radar," *IEEE Trans. Geosci. Remote Sens.*, vol. GE-19, no. 2, pp. 108–116, Apr. 1981.

[29] N. Gebert, G. Krieger, and A. Moreira, "Multichannel azimuth processing in ScanSAR and TOPS mode operation," *IEEE Trans. Geosci. Remote Sens.*, vol. 48, no. 7, pp. 2994–3008, Jul. 2010.

[30] R. Torres *et al.*, "GMES Sentinel-1 mission," *Remote Sens. Environ.*, vol. 120, pp. 9–24, May 2012.

[31] N. Gebert, G. Krieger, and A. Moreira, "Digital beamforming on receive: Techniques and optimization strategies for high-resolution wide-swath SAR imaging," *IEEE Trans. Aerosp. Electron. Syst.*, vol. 45, no. 2, pp. 564–592, Apr. 2009.

[32] D. Zheng and F. Da, "A novel algorithm for branch cut phase unwrapping," *Opt. Lasers Eng.*, vol. 49, no. 5, pp. 609–617, May 2011.

[33] K. Desai, P. Joshi, S. Chirakkal, D. Putrevu, and R. Ghosh, "Analysis of performance of flat Earth phase removal methods," *ISPRS-Int. Arch. Photogramm., Remote Sens. Spatial Inf. Sci.*, vol. XLII-5, pp. 207–209, Nov. 2018.

[34] A. M. Guarnieri and C. Prati, "Sar interferometry: A 'quick and dirty' coherence estimator for data browsing," *IEEE Trans. Geosci. Remote Sens.*, vol. 35, no. 3, pp. 660–669, May 1997.

TIANWEN LUO received the B.S. degree in surveying and mapping engineering from Xi'an Jiaotong University, China, in 2003, and the M.S. degree in surveying and mapping engineering from the China University of Geosciences, Wuhan, China, in 2008. He is currently pursuing the Ph.D. degree in geodesy and surveying engineering with Wuhan University, China.

His research interests include deformation monitoring with GNSS and InSAR

FEI LI received the B.S. degree from the University of Science and Technology of China, Hefei, China, in 1982, and the Ph.D. degree from the Institute of Geodesy and Geophysics of Chinese Sciences Academy, Wuhan, China, in 1992.

He is currently a Professor with the State Key Laboratory of Information Engineering in Surveying, Mapping and Remote Sensing, Wuhan University, Wuhan. He is also the Vice President of Wuhan University. His research interests include geodesy and geophysics.

BIN PAN received the B.S. and M.S. degrees in photogrammetry and remote sensing from the Wuhan Technical University of Surveying and Mapping, Wuhan, China, in 1994 and 1999, respectively, and the Ph.D. degree in photogrammetry and remote sensing from Wuhan University, Wuhan, in 2010. From 1994 to 1996, he was a Teaching Assistant with the Department of Aero Photogrammetry, Wuhan Technical University of Surveying and Mapping, where he was a Lecturer, till 1999. From 2000 to 2004, he was a Lecturer with the School of Remote Sensing and Information Engineering, Wuhan University, where he was an Associate Professor, till 2009 and has been a Professor, since 2010. He has coauthored two books, more than 20 articles, and more than ten inventions. His research interests include synthetic aperture radar (SAR) remote sensing theory and method, and SAR interferometry theory and its application in small distortion detection of the Earth's surface caused by subsidence and geologic hazard.

T. Luo *et al.*: Deformation Monitoring of Slopes With a Shipborne InSAR System: A Case Study of the Lancang River Gorge

IEEE *Access*

WEI ZHOU received the B.S., M.S., and Ph.D. degrees from Wuhan University, China, in 1998, 2001, and 2004, respectively, all in hydraulic structure engineering.

He is currently a Professor with the School of Water Resources and Hydropower Engineering, Wuhan University. His research interests include micromechanics of granular materials, computational geomechanics-combined FEM and DEM, discontinuum modeling to fracture, fragmentation and granular processes for rock and concrete, multi-scale mechanics from micro to macro.

GUANGBAO SHEN received the B.S. degree in remote sensing science and technology from Wuhan University, Wuhan, China, in 2019, where he is currently pursuing the M.S. degree in photogrammetry and remote sensing. His research interests include synthetic aperture radar (SAR) data processing field and SAR interferometry theory and its application to the Earth's surface displacement monitoring.

HONGJIE CHEN received the Ph.D. degree in geotechnical engineering from Hehai University, China, in 2014. He is mainly engaged in the scientific research on the safety construction and management of hydropower projects. In recent years, he mainly focused on the non-contact deformation monitoring technology of the landslide on the reservoir bank.

WEIFENG HAO received the M.S. degree from the Central South University, China, in 2008, and the Ph.D. degree from Wuhan University, Wuhan, China, in 2012, all in geodesy and surveying engineering.

He is currently an Associate Professor with the Chinese Antarctic Center of Surveying and Mapping, Wuhan University. His research interests include data processing of satellite altimetry, and satellite gravity and their applications.

● ● ●